

Multiscale Mixed Methods on Corner-Point Grids: Mimetic versus Mixed Subgrid Solvers

Jørg E. Aarnes, Stein Krogstad, Knut–Andreas Lie, and Vsevolod Laptev

ABSTRACT. Multiscale simulation is a promising approach to facilitate direct simulation of large and complex grid-models for highly heterogeneous petroleum reservoirs. Unlike traditional simulation approaches based on upscaling/downscaling, multiscale methods seek to solve the full flow problem by incorporating sub-scale heterogeneities into local discrete approximation spaces. We consider a multiscale formulation based on a hierarchical grid approach, where basis functions with subgrid resolution are computed numerically to correctly and accurately account for subscale variations from an underlying (fine-scale) geomodel when solving the global flow equations on a coarse grid. By using multiscale basis functions to discretise the global flow equations on a (moderately-sized) coarse grid, one can retain the efficiency of an upscaling method, while at the same time produce detailed and conservative velocity fields on the underlying fine grid.

For pressure equations, the multiscale mixed finite-element method (MsMFEM) has shown to be a particularly versatile approach. In this paper we extend the method to corner-point grids, which is the industry standard for modelling complex reservoir geology. To implement MsMFEM, one needs a discretisation method for solving local flow problems on the underlying fine grids. To this end, we propose two different subsolvers that both are designed to give accurate and robust discretisations with minimal grid-orientation effects on grids with strong anisotropies and irregular geometries. Our first subsolver subdivides the hexahedral corner-point cells into a set of tetrahedra, on which a standard mixed finite-element method is used. Our second subsolver is based on mimetic discretisation principles and works directly on the hexahedral cells. A mimetic discretisation is a generalisation of mixed finite elements that gives a discrete inner product and allows for curved grid faces and polyhedral elements.

The versatility and accuracy of the multiscale mixed methodology is demonstrated on two corner-point models: a small Y-shaped sector model and a complex model of a layered sedimentary bed. In particular, we demonstrate how one can avoid the usual difficulties of resampling, when moving from a fine to a coarse grid, and vice versa, since the multiscale mixed formulation allows the cells in the coarse grid to be chosen as an (almost) arbitrary connected collection of cells in the underlying fine grid.

1. Introduction

Rock formations found in natural petroleum reservoirs are typically heterogeneous at all length scales, from the micrometre scale of pore channels between sand grains to the kilometre scale of the full reservoir. However, when modelling fluid flow in porous formations, it is generally not possible to account for all pertinent scales that impact the flow. Instead one has to create models for studying phenomena occurring at a reduced span of scales. In reservoir engineering, the reservoir is modelled in terms of a three-dimensional grid, in which the layered structure of sedimentary beds (a small unit of rock distinguishable from adjacent rock units) in the reservoir is reflected in the geometry of the grid cells. The physical properties of the rock (porosity and permeability) are represented as constant values inside each grid cell.

Modern methods for 3D geological modelling and reservoir characterisation is leading industry to routinely build very large and detailed reservoir models; grid models of the subsurface geology currently range in size from 10 to 100 million cells and are growing. Moreover, the industry is moving away from a single “best effort” modelling and towards computations of many plausible realisations to assess uncertainty in geomodels. Due to the highly heterogeneous nature of

porous rock formations, geomodels tend to have strongly irregular geometries and very complex hydraulic connectivities. Unfortunately, reservoir simulation technology has not kept pace with the development within geological modelling, and there is a steadily increasing gap between the level of detail seen in industrial geomodels and the capabilities of current flow simulators. In part, industry-standard simulators are incapable of simulating models with multi-million cells, and, in part, the underlying discretisation methods were not designed to handle the challenges posed by current geomodels: high aspect ratios, anisotropic properties, curved faces, degenerate cells, non-conformal grids, etc.

The traditional approach to overcome the gap in resolution between geomodels and simulation models is to use upscaling/downscaling between a detailed geological model and a coarser simulation model. In this paper we will discuss an alternative approach based on a multiscale formulation for computing pressure and flow velocities, where the full flow problem is solved by incorporating sub-scale heterogeneities into local discrete approximation spaces. This means that the global flow is computed on a coarse grid and fine-scale heterogeneity is accounted for through a set of generalised, heterogeneous basis functions. The basis functions are computed numerically by solving local flow problems (as is done in many flow-based upscaling methods), and when included in the coarse-grid equations, the basis functions ensure that the global equations are consistent with the local properties of the underlying differential operators. By using the multiscale basis functions to discretise the flow equations on a (moderately-sized) coarse grid, one can retain the efficiency of an upscaling method and at the same time produce detailed and conservative velocity fields.

The multiscale mixed finite-element formulation [11, 1, 3] has previously shown to be a particularly versatile approach for flow simulation on Cartesian grids in the sense that it produces more accurate and robust results than what is obtained by traditional upscaling approaches; see [2]. Here we take the important step of extending the methodology to the more complex corner-point grid format used in the oil industry. In particular, we seek to demonstrate that by using a multiscale formulation one avoids the usual difficulties of resampling grid properties when moving from a fine to a coarse grid, and vice versa. In the multiscale formulation, the cells in the coarse grid can, at least in principle, be chosen as an almost arbitrary connected collection of cells in the underlying fine grid.

The outline of the paper is as follows. We start by discussing the complexity of geological grid models and some of the challenges they pose for flow simulation in Section 2. In Section 3, we present our basic flow model and its mixed formulation and before we introduce the multiscale method in Section 4. In Section 5, we present two alternative subgrid discretisation techniques that will be used to construct basis functions for the multiscale method. Finally, we present and discuss two numerical examples in Section 6 to highlight some of the properties of the multiscale method. In particular, we compare the multiscale velocity fields obtained on different coarse grids using the two alternative discretisation techniques as subgrid solvers and solve a two-phase flow equation on the underlying fine grid to see how strongly discrepancies in the velocity fields impact flow characteristics.

2. Complexity of Reservoir Simulation Models

Natural petroleum reservoirs typically consist of a subsurface body of sedimentary rock having sufficient porosity and permeability to store and transmit fluids. Sedimentary rocks are formed through deposition of sediments and typically have a layered structure with different mixtures of rock types. In its simplest form, a sedimentary rock consists of a stack of sedimentary beds that extend in the lateral direction. Due to differences in deposition and compaction, the thickness and inclination of each bed will vary in the lateral directions. In fact, during the deposition, parts of the beds may have been weathered down or completely eroded away. In addition, the layered structure of the beds may have been disrupted due to geological activity, introducing fractures and faults. Fractures are cracks or breakage in the rock, across which there has been no movement. Faults are fractures across which the layers in the rock have been displaced.

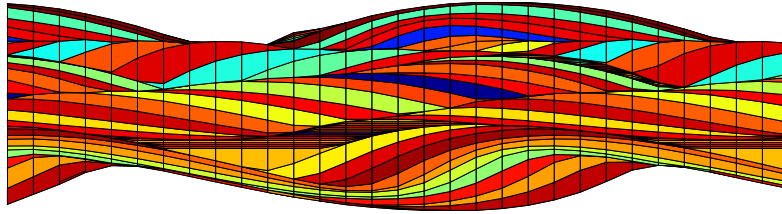


FIGURE 1. Side view in the xz -plane of corner-point grid with vertical pillars modelling a stack of sedimentary beds (each layer indicated by a different colour).

To model such geological structures, a standard approach is to introduce what is called a corner-point grid [15]. A corner-point grid consists of a set of hexahedral cells that are aligned in a logical Cartesian fashion. One horizontal layer in the grid is then assigned to each sedimentary bed to be modelled. In its simplest form, a corner-point grid is specified in terms of a set of vertical or inclined pillars defined over an areal Cartesian 2D mesh in the lateral direction. Each cell in the volumetric corner-point grid is restricted by four pillars and is defined by specifying the eight corner points of the cell, two on each pillar. Figure 1 shows a side-view of such a corner-point grid. Notice the occurrence of degenerate cells with less than eight non-identical corners where the beds are partially eroded away. Some cells also disappear completely and hence introduce new connections between cells that are not neighbours in the underlying logical Cartesian grid.

The corner-point format easily allows for degeneracies in the cells and discontinuities (fractures/faults) across faces. Hence, using the corner-point format it is possible to construct very complex geological models that match the geologist's perception of the underlying rock formations. Due to their many appealing features, corner-point grids are now an industry standard and the format is supported in most commercial software for reservoir modelling and simulation. The original corner-point format has been extended in several directions, for instance to allow intersection of two straight pillars in the shape of the letter Y. Similarly, the pillars may be piecewise polynomial curves, resulting in what is sometimes called S-faulted grids.

Using geological models as input to flow simulation introduces several numerical difficulties. First of all, typical reservoirs extend several hundred or thousand metres in the lateral direction, but the zones carrying hydrocarbon may be just a few tens of metres in the vertical direction and consist of several layers with different rock properties. Geological models therefore have grid-cells with very high aspect ratios and often the majority of the flow in and out of a cell occurs across the faces with the smallest area. Similarly, the possible presence of strong heterogeneities and anisotropies in the permeability fields typically introduces large condition numbers in the discretised flow equations. These difficulties are observed even for grid models consisting of regular hexahedral cells.

The flexible cell geometry of the corner-point format introduces additional difficulties. First of all, since each face of a grid cell is specified by four (arbitrary) points, the cell interfaces in the grid will generally be bilinear surfaces and possibly be strongly curved. Secondly, corner-point cells may have zero volume, which introduces coupling between non-neighbouring cells and gives rise to discretisation matrices with complex sparsity patterns. Similarly, for cells with almost zero volume there will be very large differences in the areas of the cell faces, meaning that large amounts of flow in the numerical solution may be forced through faces with almost zero area. Finally, the presence of degenerate cells, in which the corner-points collapse in pairs, means that the cells will generally be polyhedral and possibly contain both triangular and bilinear faces (see Figure 2). This calls for a very flexible discretisation that is not sensitive to the geometry of each cell or the number of faces and corner points.

To model pressure and velocities, most commercial reservoir simulators use traditional finite-difference methods like the two-point flux approximation scheme. These methods were not designed to cope with the type of models that are now routinely built using modern geomodelling tools. Indeed, corner-point grids are generally nonorthogonal, meaning that the connections

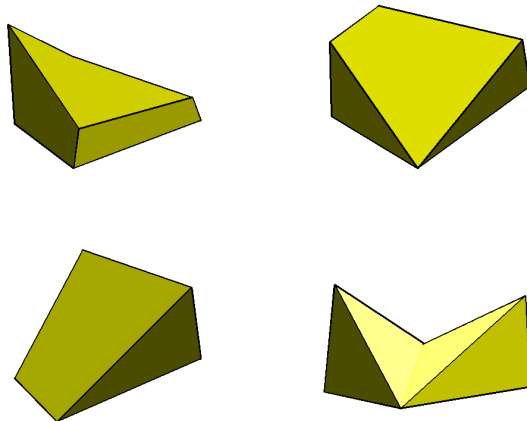


FIGURE 2. Examples of deformed and degenerate hexahedral cells arising in corner-point grid models.

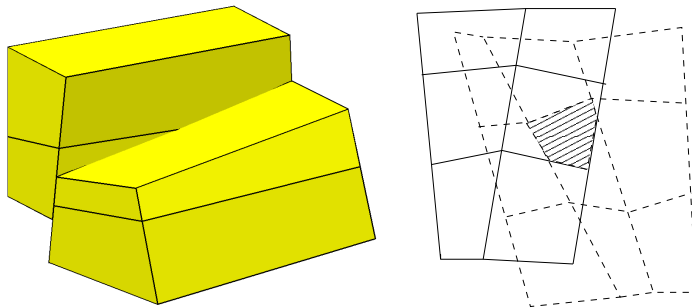


FIGURE 3. Two examples of fault surface in a three-dimensional model with non-matching interfaces across the faults. (Left) Three-dimensional view. (Right) Two-dimensional view, where the shaded patch illustrates a “sub-interface” on the fault surface.

between cell centres are not perpendicular to the cell faces. This implies that two-point flux-approximation schemes are generally not convergent. More advanced finite-difference methods [4, 5, 12] that amend the shortcomings of the two-point scheme have been developed, but these methods are generally hard to implement for general corner-point grids, especially if the grid is non-conforming with non-matching interfaces. Non-conforming grids arise, using the corner-point format, in fault zones where a displacement along a hyperplane has occurred, see Figure 3.

In this paper we employ a multiscale mixed finite-element method to model pressure and velocities in a two-phase model. To implement a multiscale mixed FEM, one needs a discretisation method for solving elliptic flow problems on the underlying fine grid to define the local multiscale basis functions. To this end, a finite-difference method may in principle be used. However, for the current purpose, we seek a method that is more accurate than the traditional two-point flux-approximation schemes, and somewhat more flexible with respect to grids than the more advanced multi-point flux-approximation schemes [4, 5, 12]. We propose two alternative approaches aimed at meeting the geometrical challenges posed by industry-standard geomodels. Our first approach is to subdivide the hexahedral corner-point cells into tetrahedra in such a way that the resulting tetrahedral grid is conforming and use a standard Raviart–Thomas mixed finite-element method as a subgrid solver on the tetrahedral subgrids. Our second approach is to consider the degenerate hexahedral as general polyhedral cells and use recent mimetic discretisation principles to build a solver that works directly on the corner-point grid.

In this paper we will only consider conformal grids. The extension of the methodology to non-conformal grid with non-matching faces, or alternatively to conforming grids with general polyhedral faces, is a topic for future research.

3. Mixed Formulation of Elliptic Model Problem

Let $\Omega \subset \mathbb{R}^3$ be a polyhedral domain, and let n be the outward unit normal on $\partial\Omega$. As a prototype flow problem, we consider the following second-order elliptic equation:

$$(1) \quad \begin{aligned} v &= -K\nabla p, & x \in \Omega, \\ \nabla \cdot v &= f, & x \in \Omega, \\ v \cdot n &= 0, & x \in \partial\Omega, \end{aligned}$$

where we require, for compatibility, that $\int_{\Omega} f \, dx = 0$. Since this is a pure Neumann boundary-value problem, p is defined only up to an arbitrary constant. An extra constraint, such as $\int_{\Omega} p \, dx = 0$, must therefore be added to close the system. Henceforth we refer to p as the pressure and v as the velocity.

To discretise (1), we introduce an arbitrary partition of Ω into polyhedral-like cells $\mathcal{T} = \{T\}$, and define the following function spaces:

$$\begin{aligned} H^{\text{div}}(T) &= \{v \in L^2(T)^d : \nabla \cdot v \in L^2(T)\}, \\ H_0^{\text{div}}(\mathcal{T}) &= \{v \in H^{\text{div}}(\cup_{T \in \mathcal{T}} T) : v \cdot n = 0 \text{ on } \partial\Omega\}, \\ H_0^{\text{div}}(\Omega) &= H_0^{\text{div}}(\mathcal{T}) \cap H^{\text{div}}(\Omega). \end{aligned}$$

Furthermore, introduce the following bilinear forms:

$$(2) \quad \begin{aligned} b(\cdot, \cdot) : H_0^{\text{div}}(\mathcal{T}) \times H_0^{\text{div}}(\mathcal{T}) &\rightarrow \mathbb{R}, & b(u, v) &= \sum_{T \in \mathcal{T}} \int_T u \cdot K^{-1} v \, dx \\ c(\cdot, \cdot) : H_0^{\text{div}}(\mathcal{T}) \times L^2(\Omega) &\rightarrow \mathbb{R}, & c(v, p) &= \sum_{T \in \mathcal{T}} \int_T p \nabla \cdot v \, dx \\ d(\cdot, \cdot) : H_0^{\text{div}}(\Omega)^d \times L^2(\partial\mathcal{T}) &\rightarrow \mathbb{R}, & d(v, \pi) &= \sum_{T \in \mathcal{T}} \int_{\partial T} \pi v \cdot n_T \, ds \\ (\cdot, \cdot) : L^2(\Omega) \times L^2(\Omega) &\rightarrow \mathbb{R}, & (p, q) &= \int_{\Omega} pq \, dx. \end{aligned}$$

Here n_T is the unit normal on ∂T pointing outward. We will now use these bilinear forms to develop a discretisation based on a mixed formulation. The mixed formulation will later be used for two purposes. Primarily, it will be used to formulate the multiscale mixed finite-element method to be introduced in Section 4. Secondly, the mixed formulation will be used in Section 5 to develop mixed finite-element and mimetic finite-difference discretisation schemes for the subgrid problems arising in the multiscale formulation.

3.1. Mixed Formulation. In the general mixed formulation of (1), one seeks a pair of functions $(p, v) \in L^2(\Omega) \times H_0^{\text{div}}(\Omega)$ such that

$$(3) \quad \begin{aligned} b(u, v) - c(u, p) &= 0, & \forall u \in H_0^{\text{div}}(\Omega), \\ c(v, q) &= (f, q), & \forall q \in L^2(\Omega). \end{aligned}$$

In mixed FEMs, the system (3) is discretised by replacing $L^2(\Omega)$ and $H_0^{\text{div}}(\Omega)$ with finite-dimensional subspaces U and V . One then seeks approximations $p \in U$ and $v \in V$ that satisfy (3) for all test functions $q \in U$ and $u \in V$. A typical example of subspaces is the lowest-order Raviart–Thomas functions, for which U is the space of piecewise constants $\mathcal{P}_0(\mathcal{T})$ and V is given by

$$V \subset \{u \in H_0^{\text{div}}(\Omega) \mid \nabla \cdot u \in U, u \cdot n_T = \text{const}\}.$$

The discretised problem admits a unique solution if there exist constants $C_1, C_2 > 0$ such that

$$(4) \quad b(v, v) \geq C_1 \|v\|_{H_0^{\text{div}}(\Omega)}^2, \quad \forall v \in Z, \quad (Z\text{-ellipticity}),$$

where $Z = \{v \in V : c(v, p) = 0, \forall p \in U\}$, and

$$(5) \quad \sup_{v \in V} \frac{c(v, p)}{\|v\|_{H_0^{\text{div}}(\Omega)}} \geq C_2 \|p\|, \quad \forall p \in U \quad (\text{inf-sup condition}).$$

Here $\|\cdot\|$ denotes the L^2 norm. If (4)–(5) hold for positive constants C_1 and C_2 , independent of mesh resolution, we say that U and V satisfy the *Babuška–Brezzi* (BB) condition. The inf-sup condition alone is sometimes called the *Ladyzhenskaya–Babuška–Brezzi* (LBB) condition.

A mixed FEM solution (p, v) of (3) in $U \times V$ is a saddle-point of the following Lagrange functional:

$$L(v, p) = \frac{1}{2}b(v, v) - c(v, p) + (p, f).$$

This means that $L(v, q) \leq L(v, p) \leq L(u, p)$. Consequently, mixed FEM discretisations lead to indefinite linear systems. Indefinite systems require special linear solvers and are often considered hard to solve. Next, we therefore introduce an alternative formulation of the mixed method that will give a positive definite discret system and thereby simplify the computation of a discrete solution.

3.2. Hybrid Formulation. In a hybrid formulation [6], the need to solve a saddle-point problem is avoided by using Lagrange multipliers. The hybrid formulation is therefore sometimes called the Lagrange multiplier technique. For (1), the hybrid formulation is obtained by replacing the mixed formulation (3) with the following problem: find $(v, p, \pi) \in H_0^{\text{div}}(\mathcal{T}) \times L^2(\Omega) \times L^2(\partial\mathcal{T} \setminus \partial\Omega)$ such that

$$(6) \quad \begin{aligned} b(u, v) - c(u, p) + d(u, \pi) &= 0, & \forall u \in H_0^{\text{div}}(\mathcal{T}), \\ c(v, q) &= (f, q), & \forall q \in L^2(\Omega), \\ d(v, \mu) &= 0, & \forall \mu \in L^2(\partial\mathcal{T} \setminus \partial\Omega). \end{aligned}$$

Here $\partial\mathcal{T} = \cup_{T \in \mathcal{T}} \partial T$ and the new unknowns π correspond to pressures at element faces. To discretise (6), one selects finite-dimensional subspaces $V \subset H_0^{\text{div}}(\mathcal{T})$, $U \subset L^2(\Omega)$, and $\Pi \subset L^2(\partial\mathcal{T} \setminus \partial\Omega)$, and seeks $(v, p, \pi) \in V \times U \times \Pi$ such that (6) holds for all $(u, q, \mu) \in V \times U \times \Pi$. Observe that in this approach one departs from the constraint $V \subset H^{\text{div}}(\Omega)$. Instead flux continuity is enforced through the Lagrange multipliers. In other words, the idea is to first remove the constraint that the normal velocity must be continuous across element faces and integrate (1) to get a weak form containing jump terms at block boundaries. Continuity of the normal component is then reintroduced by adding an extra set of equations, where the pressure π at the interfaces plays the role of Lagrange multipliers. This procedure does not change v , nor p , but enables the recovery of pressure values at element faces, in addition to inducing the desired change in structure of the linear system resulting from the discretisation.

3.3. Mimetic Formulation. Recent mimetic finite-difference methods (FDMs) [10, 9] can be seen as finite-difference counterparts of mixed FEMs. The discretisation in a standard mixed method is introduced by picking discrete function spaces U_h and V_h and using numerical quadrature to evaluate the integrals over cell volumes and cell faces in the variational formulation (3). In a mixed method, the discretisation is introduced already in the variational formulation in the form of a discrete innerproduct. Mathematically, this means that the subspace V in $H_0^{\text{div}}(\Omega)$ is replaced by a discrete subspace of $L^2(\partial\mathcal{T})$, and the associated bilinear form $b(\cdot, \cdot)$ is replaced by a bilinear form that acts on $L^2(\partial\mathcal{T}) \times L^2(\partial\mathcal{T})$. This means that instead of seeking an unknown velocity field v defined over each element T , one seeks a set of fluxes defined over the cell faces ∂T .

The most apparent advantage of mimetic FDMs relative to mixed FEMs, is the ability to handle complex polyhedral grids cells (with strongly curved faces [9]) in a straightforward manner. Stability and optimal convergence of mimetic FDMs were established by [7, 8] for very general grids. For flow in porous media, polyhedral cells arise frequently in geological models when conforming hexahedral corner-point grids are deformed to model geological phenomena like erosion and pinch-outs. Similarly, for corner-point grids containing faults and throws, one can subdivide grid faces and turn the non-conforming corner-point grids into conforming polyhedral grids. However, in the current paper we only consider conforming corner-point grids. We will return to the

discrete formulation of mimetic FDM in Section 5.1 and introduce a particular variant [10] that closely resembles the lowest-order Raviart–Thomas MFEM for hexahedral cells.

In the hybrid formulation of a mimetic FDM, one only needs to replace V with a discrete subspace $M \subset L^2(\partial\mathcal{T})$, and $b(\cdot, \cdot)$ with a bilinear form $m(\cdot, \cdot)$ that acts on $L^2(\partial\mathcal{T}) \times L^2(\partial\mathcal{T})$.

3.4. Discrete Formulations. The algebraic systems that arise from mixed finite-element or mimetic finite-difference discretisations of (1) take the same general form, whether we employ a standard or a hybrid formulation. In this paper we employ a hybrid formulation only. The hybrid formulation (6) gives rise to linear systems of the following form:

$$(7) \quad \begin{bmatrix} \mathbf{B} & -\mathbf{C}^T & \mathbf{\Pi}^T \\ \mathbf{C} & \mathbf{0} & \mathbf{0} \\ \mathbf{\Pi} & \mathbf{0} & \mathbf{0} \end{bmatrix} \begin{bmatrix} \mathbf{v} \\ \mathbf{p} \\ \pi \end{bmatrix} = \begin{bmatrix} \mathbf{0} \\ \mathbf{f} \\ \mathbf{0} \end{bmatrix}.$$

In the mixed FEMs and the mimetic FDM considered herein, the approximation space U consists of functions that are cell-wise constant

$$U = \text{span}\{\chi_m : T_m \in \mathcal{T}\}, \quad \chi_m(x) = \begin{cases} 1, & \text{if } x \in T_m, \\ 0, & \text{otherwise.} \end{cases}$$

Consequently, for $v \in H_0^{\text{div}}(\mathcal{T})$ and $p \in U$, we have

$$c(v, p) = \sum_m p_m \int_{T_m} \nabla \cdot v \, dx = \sum_m p_m \int_{\partial T_m} v \cdot n_T \, ds.$$

This shows that $c(v, p)$ can be evaluated without having an explicit representation of the velocity inside each cell, only values on the cell boundaries are needed. Clearly, this is the case also for $d(v, \pi)$ for any $\pi \in \Pi \subset L^2(\partial\mathcal{T})$. We therefore assume that Π consists of functions that are constant on each grid face, i.e.,

$$\Pi = \text{span}\{\pi_j^i : |\gamma_j^i| > 0, \gamma_j^i = \partial T_i \cap \partial T_j\}, \quad \pi_j^i(x) = \begin{cases} 1, & \text{if } x \in \gamma_j^i, \\ 0, & \text{otherwise.} \end{cases}$$

To derive a discrete formulation, it only remains to define an approximation space for velocity V for the mixed FEM, or alternatively a discrete approximation space $M \subset L^2(\partial\mathcal{T})$ and a corresponding bilinear form $m(\cdot, \cdot)$ to be used in a mimetic FDM. This will be done in subsequent sections. For now, we only assume that a “velocity” basis function ψ_i^m is associated with each face γ_i^m of every grid cell T_m . Thus, whereas we have one Lagrange multiplier for each “interface”, we have a velocity basis function for each face of every grid cell. Note that ψ_i^m lives in different spaces, depending on whether a mixed FEM or a mimetic FDM is used.

The matrices \mathbf{C} and $\mathbf{\Pi}$ in (7) are now given by

$$\mathbf{C} = [c(\psi_i^m, \chi_n)] \quad \text{and} \quad \mathbf{\Pi} = [d(\psi_k^m, \mu_j^i)],$$

and the matrix \mathbf{B} is given by

$$\mathbf{B} = [b(\psi_i^m, \psi_j^n)], \quad \mathbf{B} = [m(\psi_i^m, \psi_j^n)]$$

for the mixed FEM and the mimetic FDM, respectively.

The hybrid system (7) is indefinite, but $b(\psi_i^m, \psi_j^n)$ and $m(\psi_i^m, \psi_j^n)$ are nonzero only if $n = m$. Hence, by numbering the basis functions ψ_i^m on a cell-by-cell basis, the matrix \mathbf{B} becomes block diagonal, and a Schur-complement reduction with respect to \mathbf{B} can be performed to obtain the following positive-definite system for \mathbf{p} and π :

$$(8) \quad \begin{bmatrix} \mathbf{D} & -\mathbf{F}^T \\ \mathbf{F} & -\mathbf{\Pi B}^{-1} \mathbf{\Pi}^T \end{bmatrix} \begin{bmatrix} \mathbf{p} \\ \pi \end{bmatrix} = \begin{bmatrix} \mathbf{f} \\ \mathbf{0} \end{bmatrix},$$

where $\mathbf{D} = \mathbf{C B}^{-1} \mathbf{C}^T$ and $\mathbf{F} = \mathbf{\Pi B}^{-1} \mathbf{C}^T$.

Next, we use the fact that $c(\psi_i^m, \chi_n) \neq 0$ only if $n = m$ to deduce that \mathbf{D} is a diagonal matrix. A Schur-complement reduction with respect to \mathbf{D} can therefore be performed to yield the following positive-definite system for π alone:

$$(9) \quad \mathbf{S} \pi = \mathbf{F D}^{-1} \mathbf{f}, \quad \text{where} \quad \mathbf{S} = \mathbf{\Pi B}^{-1} \mathbf{\Pi}^T - \mathbf{F D}^{-1} \mathbf{F}^T.$$

Once π is computed, one can easily compute \mathbf{p} and \mathbf{v} by solving a diagonal and a block-diagonal system respectively.

4. A Multiscale Mixed Finite-Element Method

Our motivation for introducing mixed and mimetic methods on corner-point grids, is that they allow an easy implementation of multiscale mixed FEMs on coarsened grids. For instance, geological reservoir models (which are typically corner-point grid models) may contain multi-million grid cells, and a direct solution of the elliptic (or parabolic) pressure equation will generally be infeasible. Instead, it is often sufficient to model the flow on a coarse scale as long as the velocity field preserves important fine-scale features such as narrow high-permeable flow channels. Narrow high-flow channels will usually go unresolved in upscaled models, but are adequately modelled within a multiscale framework, even though the flow equations are solved on a coarse grid.

The multiscale mixed FEM (MsMFEM) was first introduced by Chen and Hou [13] and gave mass-conservative velocity fields on the discretisation grid (the coarse grid). Below, we outline a variant of MsMFEM developed by Aarnes [1, 2, 3] that also provides a mass-conservative velocity field on an underlying subgrid. In fact, the fine-scale velocities define a conservative velocity field on *any* grid consisting of a simply-connected union of cells from the fine grid. Thus, the grid used to simulate fluid transport does not have to coincide with the coarse grid in the multiscale method or with the underlying fine grid. The multiscale method can therefore easily be combined with adaptive strategies for solving the fluid transport equations.

In multiscale mixed FEMs one attempts to design basis functions for velocity that embody the local impact of subgrid variations in the permeability K . To formulate MsMFEM, let $\mathcal{B} = \{B\}$ be a grid where each grid block B is a connected union of grid cells in an underlying subgrid \mathcal{T} . The grid \mathcal{B} will be referred to as the *coarse grid*, and the subgrid \mathcal{T} will be referred to as the *fine grid*. For each interface $\Gamma_{ij} = \partial B_i \cap \partial B_j$ in the coarse grid, we assign a corresponding basis function Ψ_{ij} . This basis function is related to an unknown function Φ_{ij} through the gradient relation $\Psi_{ij} = -K\nabla\Phi_{ij}$. The function Φ_{ij} is supported in $\Omega_{ij} = B_i \cup \Gamma_{ij} \cup B_j$ and is obtained by solving (numerically) a local elliptic problem

$$(10) \quad \Psi_{ij} \cdot n_{ij} = 0 \text{ on } \partial\Omega_{ij}, \quad \nabla \cdot \Psi_{ij} = \begin{cases} f_i(x), & \text{for } x \in B_i, \\ -f_j(x), & \text{for } x \in B_j. \end{cases}$$

Here n_{ij} is the outward-pointing unit normal to Ω_{ij} , and the source terms f_i and f_j are given by

$$(11) \quad f_i(x) = \frac{w_i(x)}{\int_{B_i} w_i(x) dx}, \quad w_i = \begin{cases} f, & \text{if } \int_{B_i} f dx \neq 0, \\ \text{trace}(K), & \text{otherwise.} \end{cases}$$

The source terms $\{f_i\}$ are defined as in (11) for the following reasons. First, with this definition, the basis function Ψ_{ij} forces unit flux across Γ_{ij} ; that is, $\int_{\Gamma_{ij}} \psi_{ij} \cdot n ds = 1$, where n is the unit normal of Γ_{ij} pointing into B_j . This implies that the velocity solution $\{v_{ij}\}$ gives the fluxes across the respective coarse-grid interfaces. Second, if a conservative method is used to compute basis functions, the velocity $v = \sum v_{ij} \psi_{ij}$ conserves mass on the subgrid \mathcal{T} . Third, choosing special source terms in blocks containing nonzero source terms allows the method to model radial flow around point or line sources, such as wells in oil-reservoirs, on the subgrid scale. Finally, by letting f_i scale according to the trace of K , as in (11), one can to some extent avoid unnaturally high velocities across flow barriers, see [3].

5. Subgrid Discretisation Methods

To implement MsMFEM requires that one is able to discretise the flow problems (10) over the fine grid, which may have cells with less than eight unique corners, as illustrated in Figure 2. Since cells with five to seven corners are not diffeomorphic to the unit cube, one cannot use a straightforward mixed FEM relying on a transformation from hexahedral cells back to the unit cube. Instead, one must introduce special reference elements and corresponding Piola transforms for each of the degenerate cases, and this complicates the implementation of a mixed FEM considerably.

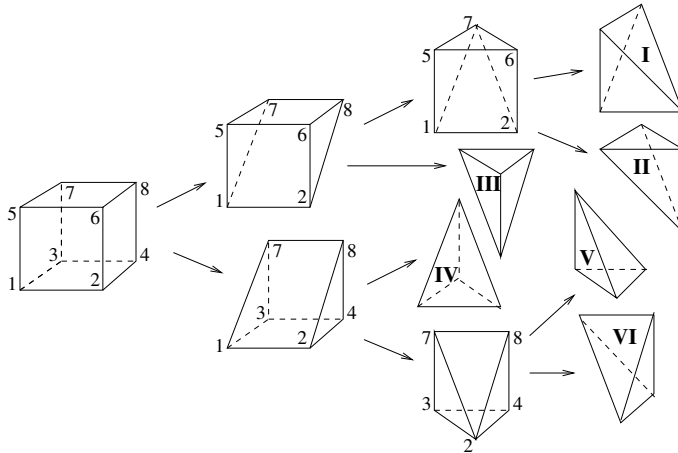


FIGURE 4. Subdivision of a hexahedral cell into six tetrahedra.

Here we therefore consider two alternative approaches. The first approach introduces a conforming tetrahedral subdivision of the corner-point grid and uses the lowest-order Raviart–Thomas MFEM to discretise (10). To partition the grid, we simply subdivide each corner-point cell as depicted in Figure 4, and then remove all tetrahedra with zero volume. In the second approach, we use a mimetic FDM directly on the fine corner-point grids to generate basis functions for the MsMFEM.

We would like to point out that by subdividing corner-point cells into tetrahedra, we assume implicitly that interfaces in the corner-point grid can be described as the union of two planar triangles. Although mimetic FDMs can handle curved interfaces also, the method presented below models interfaces in the same way. The convention in reservoir simulation is to assume that interfaces are bilinear surfaces. Thus, what we consider to be a corner-point cell here is not according to common practice, but we believe that the fact that we define the grid differently is a minor cause of concern. Indeed, geological reservoir models are a result of non-deterministic modelling approaches, and the associated corner-point grid is populated with permeabilities from a stochastic distribution. In fact, the precise form of the interfaces is not an issue in reservoir modelling. The assumption that interfaces are bilinear is therefore, in our opinion, invoked only to facilitate numerical treatment of reservoir simulation models.

5.1. A Mimetic FDM for Corner-Point Grids. In this subsection we describe the ideas of the mimetic FDMs in [10]. To this end, denote by \mathcal{F}_m the set of faces of T_m , and expand v and u in the basis $\{\psi_i^m : F_i \in \mathcal{F}_m, T_m \in \mathcal{T}\}$:

$$v = \sum_{i,m} v_i^m \psi_i^m \quad \text{and} \quad u = \sum_{i,m} u_i^m \psi_i^m.$$

Since $b(\psi_i^m, \psi_j^n)$ is nonzero only if $n = m$, we may write

$$(12) \quad b(u, v) = \sum_{T_m \in \mathcal{T}} \mathbf{u}_m^T \mathbf{B}_m \mathbf{v}_m,$$

where \mathbf{B}_m is the block diagonal of \mathbf{B} associated with T_m , and $\mathbf{v}_m, \mathbf{u}_m \in \mathbb{R}^{N_m}$ and N_m is the number of faces of T_m . The main idea in mimetic FDMs is to define matrices \mathbf{M}_m so that $(\cdot, \cdot)_{\mathbf{M}_m} = (\mathbf{M}_m(\cdot), \cdot)$ defines inner-products that *mimic* the corresponding inner-products $(\cdot, \cdot)_{\mathbf{B}_m} = (\mathbf{B}_m(\cdot), \cdot)$ associated with the continuous bilinear form $b(\cdot, \cdot)$, but which do not require explicit representations of the velocity in each cell.

In the current presentation, we assume that v_i^m represents the total flux out of T_m across $F_i \subset \mathcal{F}_m$:

$$(13) \quad v_i^m = \int_{F_i} v(s) \cdot n \, ds, \quad F_i \in \mathcal{F}_m.$$

Brezzi et al. [7] established that, in addition to symmetry, the following conditions are sufficient to ensure stability and convergence in pressure and velocity of the mimetic FDM for very general polygons:

- (1) There exist positive constants¹ s_* and S^* such that

$$(14) \quad s_* |T_m| \mathbf{v}^T \mathbf{v} \leq (\mathbf{v}, \mathbf{v})_{\mathbf{M}_m} \leq S^* |T_m| \mathbf{v}^T \mathbf{v},$$

for all $T_m \in \mathcal{T}$ and $\mathbf{v} \in \mathbb{R}^{N_m}$.

- (2) For every $T_m \in \mathcal{T}$, every \mathbf{v}_m obtained by inserting $v = K \nabla p$ into (13) for a linear function p on T_m , and every $\mathbf{u}_m \in \mathbb{R}^{N_m}$, we have

$$(15) \quad (\mathbf{v}_m, \mathbf{u}_m)_{\mathbf{M}_m} + \left(\sum_{i=1}^{N_m} u_m^{(i)} \right) \int_{T_m} p \, dx = \sum_{i=1}^{N_m} \frac{u_m^{(i)}}{|F_i|} \int_{F_i} p \, ds.$$

These conditions state that there should exist a global bound on the eigenvalues of all \mathbf{M}_m , and that the inner-products $(\cdot, \cdot)_{\mathbf{M}_m}$ should obey the Gauss–Green formula for linear pressure. A direct consequence is that the method will be exact for linear pressure; that is, the fluxes obtained by the numerical solution will match the fluxes corresponding to the exact solution.

Explicit formulae for computing \mathbf{M}_m -matrices that obey (14)–(15) in the case where the variables v_i^m represent net *face velocities* were given in [10]. Below we give the corresponding formulae for the case where the variables represent *fluxes*. To this end, let \mathbf{N}_m be the matrix whose i 'th row is defined by

$$(16) \quad \mathbf{n}_{m,i} = \frac{1}{|F_i|} \int_{F_i} n_i^T \, ds,$$

where n_i is the unit normal to face F_i pointing out of T_m ; let \mathbf{C}_m be the matrix whose i 'th row is defined by

$$(17) \quad \mathbf{c}_{m,i} = \frac{1}{|F_i|} \int_{F_i} (x - x_m)^T \, ds,$$

where x_m is the centre of T_m ; and let \mathbf{D}_m be the diagonal matrix containing the areas $|F_i|$ of each face. Finally, let \mathbf{Z}_m be a $N_m \times (N_m - d)$ matrix whose columns form an orthonormal basis for the null space of \mathbf{N}_m^T , and let \mathbf{U}_m be a symmetric positive-definite matrix of dimension $(N_m - d) \times (N_m - d)$. Then the matrix \mathbf{M}_m defined by

$$(18) \quad \mathbf{M}_m = \mathbf{M}_{m,1} + \mathbf{M}_{m,2},$$

where

$$(19) \quad \mathbf{M}_{m,1} = \frac{1}{|T_m|} \mathbf{C}_m K^{-1} \mathbf{C}_m^T, \quad \mathbf{M}_{m,2} = \mathbf{D}_m^{-1} \mathbf{Z}_m \mathbf{U}_m \mathbf{Z}_m^T \mathbf{D}_m^{-1},$$

satisfies the *discrete* Gauss–Green formula (15). In addition, some mild restrictions must be imposed on the grid and on the eigenvalues of \mathbf{U}_m in order for \mathbf{M}_m to also satisfy condition (14). We should also remark that explicit formulae for the inverse of \mathbf{M}_m (for the case where the variables represent *face velocities*) were also given in [10]. These formulae may be used to assemble \mathbf{B}^{-1} directly. This is advantageous both with respect to computational efficiency, and with respect to avoiding numerical inversion of nearly singular \mathbf{M}_m -matrices that arise for elements having one or more faces with almost zero area. The reader should consult [9, 7] for further details.

¹The bounds in this expression differ from the bounds given in [10] in the sense that we use flux unknowns rather than velocity unknowns. Thus, to obtain the constants s_*, S^* in [10], one should scale the components of \mathbf{v} by the inverse area of the corresponding faces.

Next, we motivate the form of \mathbf{M}_m given in (18), by considering multiscale basis functions similar to (10), and thus making a twist to the presentation given in [10]. Hence, for each face $F_i \subset \mathcal{F}_m$, define ψ_i by

$$(20) \quad \psi_i = -K\nabla p_i, \quad \nabla \cdot \psi_i = \frac{1}{|T_m|}, \quad \psi_i \cdot n = \begin{cases} 1/|F_i| & \text{for } x \in F_i \\ 0 & \text{for } x \in F_j. \end{cases}$$

One could now, theoretically, define the matrix \mathbf{M}_m by $[\mathbf{M}_m]_{ij} = b(\psi_i, \psi_j)$, but for general polyhedral cells, the computation of $b(\cdot, \cdot)$ is non-trivial, and thus not practical. Instead one could consider a first order approximation, i.e., find \mathbf{M}_m such that $[\mathbf{M}_m]_{ij} = b(\psi_i, \psi_j) + \mathcal{O}(h^2)$, where h is the grid-cell diameter. For this to hold true, it is sufficient to require $\mathbf{u}^T \mathbf{M}_m \mathbf{v} = b(u, v)$ whenever the sum of the polynomial orders of u and v are less or equal to one. The mimetic FDMs are based on a somewhat stricter requirement, that is, $\mathbf{u}^T \mathbf{M}_m \mathbf{v} = b(u, v)$ if one of the functions are constant, and the other is any expansion in the basis functions (20). For a constant vector field v , the corresponding vector of fluxes over the faces of T_m is given by $\mathbf{D}_m \mathbf{N}_m v$. Thus, the inner-product matrix \mathbf{M}_m must satisfy the relation

$$(21) \quad e_i^T \mathbf{M}_m \mathbf{D}_m \mathbf{N}_m e_j = b(\psi_i, e_j), \quad i = 1, \dots, N_m, \quad j = 1, 2, 3,$$

where e_i is the i -th unit vector. Since $K^{-1}e_j = \nabla((x - x_m)^T K^{-1}e_j)$, we have by the Gauss-Green theorem:

$$\int_{T_m} \psi_i^T K^{-1}e_j dx = \int_{\partial T_m} ((x - x_m)^T K^{-1}e_j) \psi_i \cdot n_i ds = e_i^T \mathbf{C}_m K^{-1}e_j.$$

It follows that \mathbf{M}_m needs to satisfy the identity $\mathbf{M}_m \mathbf{D}_m \mathbf{N}_m = \mathbf{C}_m K^{-1}$. Similarly one must have $\mathbf{N}_m^T \mathbf{D}_m \mathbf{M}_m = K^{-1} \mathbf{C}_m^T$. Following [10], we have

$$\begin{aligned} [N_m^T D_m C_m]_{ij} &= n_k^{(i)} \int_{F_k} (x^{(j)} - x_m^{(j)}) ds \\ &= \int_{\partial T_m} (x^{(j)} - x_m^{(j)}) (\nabla x_i) \cdot n ds \\ &= \int_{T_m} \nabla (x^{(j)} - x_m^{(j)}) \cdot \nabla x_i dx = \delta_{ij} |T_m|. \end{aligned}$$

Thus we have $\mathbf{N}_m^T \mathbf{D}_m \mathbf{C}_m = |T_m| \mathbf{I}$, and the form of $\mathbf{M}_{m,1}$ in (19) follows. The matrix $\mathbf{M}_{m,1}$ is obviously not positive definite, so the approach in [10] is to add a matrix $\mathbf{M}_{m,2}$ such that $\mathbf{M}_m = \mathbf{M}_{m,1} + \mathbf{M}_{m,2}$ becomes positive definite, but at the same time does not weaken the approximation properties of \mathbf{M}_m . This is obtained by choosing $\mathbf{M}_{m,2}$ such that $\mathbf{M}_m \mathbf{D}_m \mathbf{N}_m = \mathbf{M}_{m,1} \mathbf{D}_m \mathbf{N}_m$, i.e., $\mathbf{M}_{m,2} \mathbf{D}_m \mathbf{N}_m = 0$. This readily gives the form of $\mathbf{M}_{m,2}$ given in (19).

Hence, $\mathbf{M}_{m,1}$ is defined so that $b(u, v) = \mathbf{u}^T \mathbf{M}_{m,1} \mathbf{v}$ if u or v belongs to the space of constant velocities V_0 , and $\mathbf{M}_{m,2}$ is defined so that the inner-product $(\mathbf{u}, \mathbf{v})_{\mathbf{M}_m}$ is not influenced by $\mathbf{M}_{m,2}$ if either \mathbf{u} or \mathbf{v} corresponds to a constant velocity field. This leaves us only freedom to choose \mathbf{U}_m . If we view the mimetic methods as a discrete variant of the mixed finite-element method defined by the basis functions in (20), one should try to define \mathbf{U}_m so that the following equivalence relation holds:

$$(22) \quad m_*(\mathbf{v}, \mathbf{v})_{\mathbf{B}_m} \leq (\mathbf{v}, \mathbf{v})_{\mathbf{M}_m} \leq M^*(\mathbf{v}, \mathbf{v})_{\mathbf{B}_m}, \quad \forall \mathbf{v} \in \mathbb{R}^{N_m}$$

for some positive constants m_* and M^* independent of the mesh and coefficients K of the problem. Here \mathbf{B}_m is the local stiffness matrix that stems from the mixed finite-element method defined by (20). Requiring that an equivalence relation of this form should hold might imply that \mathbf{U}_m should be chosen differently for different cell geometries. However, one generally would like to be able to define \mathbf{U}_m independent of the grid. To provide some insight into how \mathbf{U}_m should be chosen if it is to be independent of cell geometries, we consider two examples.

Example I: Tetrahedral elements. For tetrahedral grids, the Raviart–Thomas MFEM space of lowest order is defined by

$$V_{\text{RT0}} = V_0 \oplus V_1,$$

where $V_1 = \{\beta(x - x_m) : \beta \in \mathbb{R}\}$. Thus, write $v = v_0 + v_1$ where $v_0 \in V_0$ and $v_1 \in V_1$. Since K is assumed to be cell-wise constant, we have

$$b(u, v) = (\mathbf{D}_m \mathbf{N}_m u_0)^T \mathbf{M}_{m,1} (\mathbf{D}_m \mathbf{N}_m v_0) + \int_{T_m} u_1^T K^{-1} v_1 dx.$$

Thus, to show that $b(u, v) = \mathbf{u}^T \mathbf{M}_m \mathbf{v}$ for all $u, v \in V_{\text{RT0}}$, we only need to show that there exists a scalar \mathbf{U}_m such that

$$\mathbf{u}_1^T \mathbf{M}_m \mathbf{v}_1 = \int_{T_m} u_1^T K^{-1} v_1 dx,$$

where \mathbf{u}_1 and \mathbf{v}_1 are the flux vectors corresponding to u_1 and v_1 respectively. To this end, observe first that if $v_1 = x - x_m$, then $\mathbf{v}_1 = \frac{3|T_m|}{4} \mathbf{I}$. Thus, since we have that $\mathbf{C}_m^T \mathbf{I} = \mathbf{0}$ for tetrahedral elements, we derive that $\mathbf{u}_1^T \mathbf{M}_m \mathbf{v}_1 = \mathbf{u}_1^T \mathbf{M}_{m,2} \mathbf{v}_1$. Next, observe that since $\nabla \cdot V_0 = 0$, we have $\mathbf{I}^T \mathbf{D}_m \mathbf{N}_m = \mathbf{0}$, and hence that $\mathbf{D}_m^{-1} \mathbf{Z}_m = \mathbf{I} / \sqrt{\sum_i |F_i|^2}$. Thus, in order to have $\mathbf{M}_m = \mathbf{B}_m$, we must define \mathbf{U}_m by

$$\mathbf{U}_m = \frac{\sum_i |F_i|^2}{9|T_m|^2} \int_{T_m} (x - x_m)^T K^{-1} (x - x_m) dx.$$

Example II: Hexahedral elements. For regular hexahedral elements (i.e., shoe-box shaped cells), the Raviart–Thomas MFEM space of lowest order is defined by

$$V_{\text{RT0}} = V_0 \oplus V_1,$$

where $V_1 = \text{span}(\{(e_j e_j^T)(x - x_m) : j = 1, 2, 3\})$ and e_j is the vector equal one in component j and zero elsewhere. For a full tensor K , we obtain with similar reasoning as above that $\mathbf{M}_m = \mathbf{B}_m$ by choosing

$$(23) \quad \mathbf{U}_m = \frac{|T_m|}{6} \text{diag}(K^{-1}), \quad \mathbf{Z}_m^T = \frac{\sqrt{2}}{2} \begin{pmatrix} 1 & 1 & 0 & 0 & 0 & 0 \\ 0 & 0 & 1 & 1 & 0 & 0 \\ 0 & 0 & 0 & 0 & 1 & 1 \end{pmatrix},$$

where $\text{diag}(K^{-1})$ denotes the diagonal part of K^{-1} . In particular, if K is isotropic, then

$$(24) \quad \mathbf{U}_m = \frac{|T_m|}{2 \text{trace}(K)} \mathbf{I}.$$

These examples indicate that \mathbf{U}_m should scale proportional to the eigenvalues of K^{-1} and proportional to the volume of $|T_m|$.

The next two subsections are devoted to demonstrating properties of the two subgrid discretisation techniques: MFEM on tetrahedral subdivisions of corner-point cells and MFDM on corner-point cells. In Section 5.2, we briefly discuss monotonicity effects for both subgrid discretisation methods for skew grids and full tensor permeabilities. In Section 5.3, we apply the MFDM to a problem with a highly oscillatory solution and try to show that accurate results are obtained by using the simple \mathbf{U}_m defined in (24) also for general corner-point grids and anisotropic permeability tensors.

5.2. Grid and Full Tensor Effects. In this section we consider effects of skew grids and full-tensor permeability for the mimetic method with \mathbf{U}_m defined by (24), and for the mixed method on a tetrahedral subgrid. Let K be the constant diagonal permeability tensor with entries $k_{xx} = 10$, $k_{yy} = 1$ and $k_{zz} = 0.1$, and let $K_\theta = R_\theta K R_\theta^T$, where R_θ is the matrix rotating the xy -plane by the angle θ . We consider the problem $\nabla \cdot K_\theta \nabla p = 0$ on $\Omega = [0, 1]^3$, with Dirichlet boundary conditions $p = 1$ for $x = 0$, $p = 0$ for $x = 1$ and zero Neumann conditions elsewhere. We remark that both methods are exact for $\theta = 0$ and $\theta = \pi/2$ as long as the grid has planar faces.

We consider a Cartesian grid and a highly distorted skew grid, both with 1 000 cells, as shown in Figure 5. In Figure 6 we have plotted the total flow-rates and maximum block-pressures for $0 \leq \theta \leq \pi/2$ for the two methods on the Cartesian grid. The maximum block-pressures are plotted as an indication of loss in monotonicity. Note that these curves should not match for the two methods since they use different grids. As seen, the two methods agree closely in total flow-rate, while a slight loss in monotonicity is observed for the tetrahedral discretisation. In Figure 7 we have plotted the corresponding results for the skew grid. Still we observe close agreement in

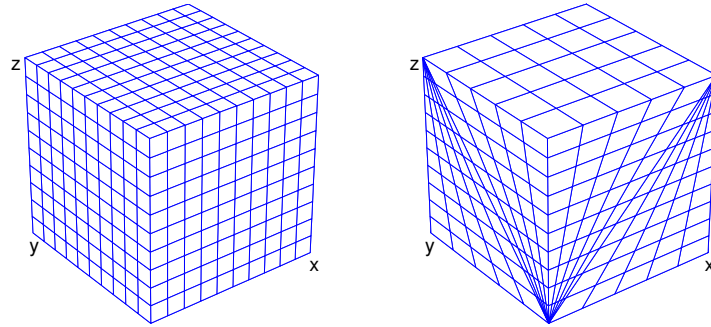


FIGURE 5. Cartesian and skew grid.

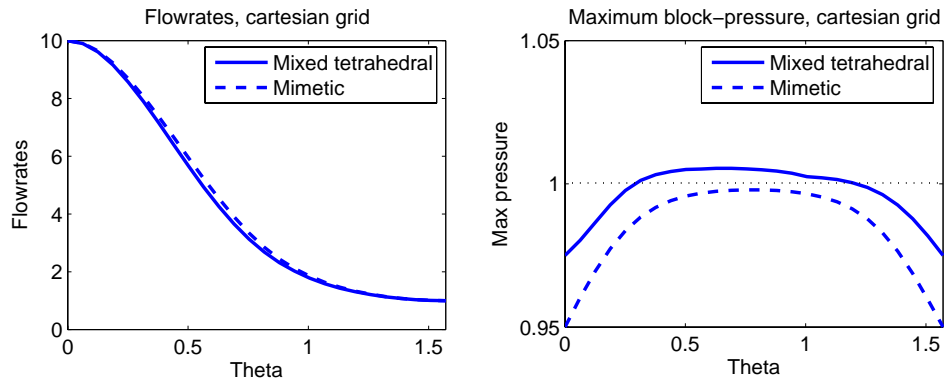


FIGURE 6. Results for various K_θ on the Cartesian grid: total flow-rate (left) and maximum block-pressure (right).

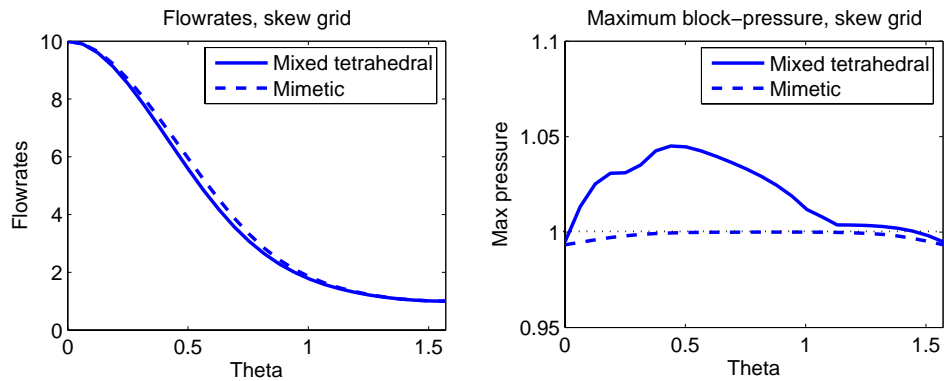


FIGURE 7. Results for various K_θ on the skew grid: total flow-rate (left) and maximum block-pressure (right).

flow-rates, while the tetrahedral discretisation over-predicts the maximal pressure by about 5%. We note that for higher anisotropy ratios, loss in monotonicity is also observed for the mimetic method for this problem.

5.3. Problems with Oscillatory Pressure Solutions. The purpose of this section is to show that to get accurate pressure solutions, it is important to choose \mathbf{U}_m so that (22) holds

TABLE 1. Pressure errors for mimetic FDM with different \mathbf{U}_m .

\mathbf{U}_m	$\frac{ T_m }{2\text{trace}(K)} \mathbf{I}$	$\frac{1}{2\text{trace}(K)} \mathbf{I}$	$\frac{ T_m }{6}$
Isotropic	$2.229 \cdot 10^{-1}$	$1.443 \cdot 10^2$	$1.443 \cdot 10^2$
Anisotropic	$2.281 \cdot 10^{-1}$	$2.445 \cdot 10^2$	$1.384 \cdot 10^1$

with constants that are nearly independent of the grid and problem coefficients. To this end, we must consider problems where the contributions from $\mathbf{M}_{m,2}$ in the local discrete inner-products are relatively large compared to the contributions from $\mathbf{M}_{m,1}$. This is achieved by considering problems with oscillating pressure solutions.

To construct a problem with an oscillating solution, we define

$$p(x, y, z) = \cos(5\pi x) \cos(5\pi y) \cos(5\pi z) \quad \text{in } \Omega = [0, 1]^3.$$

Clearly, this function oscillates rapidly in Ω . Moreover, if K is a constant diagonal tensor, we can easily show that p solves (1) with

$$f(x, y, z) = (5\pi)^2 \text{trace}(K) p(x, y, z).$$

Next, we partition Ω into a uniform $10 \times 10 \times 10$ hexahedral grid, and compute numerical pressure solutions p_h using the mimetic method with various choices of \mathbf{U}_m . We assess the accuracy of the pressure solutions relative to the exact solution p using the following measure:

$$e(p_h) = \|p_h - p\|_{L^2} / \|p_h\|_{L^2}.$$

The numerical solutions are normalised so that they have zero average in Ω . The reason why we do not compare velocity solutions is that \mathbf{U}_m has generally less influence on the velocity solutions.

We consider an isotropic case with $k_{xx} = k_{yy} = k_{zz} = 1000$, and an anisotropic case with $k_{xx} = 100$, $k_{yy} = 0.01$, and $k_{zz} = 1$. The results in Table 1 demonstrate that the mimetic FDMs can produce large errors if the matrix \mathbf{U}_m is not properly scaled. However, the results also indicate that the mimetic FDM with \mathbf{U}_m given by (24) produces pressure solutions for which the magnitude of the oscillations is about right, also in the anisotropic case.

5.4. General Remarks. We have now introduced two alternative discretisation methods for generating the velocity basis functions needed in a multiscale mixed FEM for corner-point grids. In the first method we subdivide corner-point cells into tetrahedra, and solve (10) on the tetrahedral grid using the lowest-order Raviart–Thomas MFEM. In the second method, we discretise (10) directly on the corner-point grid using mimetic finite differences.

In the mixed approach we obtain velocity fields that are mass conservative on a tetrahedral grid. This is an advantage if we are to use a streamline method to compute the fluid transport. Streamline tracing and time-of-flight computations can be done exactly for tetrahedral grids by transforming to the reference tetrahedron, since the Jacobian of the mapping from physical space to reference space is constant. On the downside, the linear systems we need to solve to generate multiscale basis functions using the mixed approach are larger than the corresponding systems for the mimetic method.

Although mimetic methods are less mature, they are quite easy to implement on complex grids and allow for a large degree of freedom in using unstructured grids consisting of general polyhedral cells to model complex geology. We believe that using a mimetic method as subgrid solver will be particularly advantageous to model flow in reservoirs with faults. Faults are usually modelled as hyperplanes, i.e., as surfaces. Across fault-faces, the corner-point grids are generally non-conforming, having non-matching interfaces, see Figure 3. A mimetic method handles grids with non-matching faces in a natural way by assigning a “basis function” for velocity to each “sub-face” $\gamma_{ij} = \partial T_i \cap \partial T_j$ of the faults. In a mixed method, flux continuity across fault-faces can be modelled using the hybrid formulation with a Lagrange multiplier (a mortar) for each “sub-face” of the fault-faces. However, although we feel that the mimetic method handles non-matching faces

in a more natural way, we will not demonstrate this flexibility with respect to non-conforming grids arising in grid-models with faults in this paper.

6. Numerical Comparisons

In this section we examine the quality of MsMFEM solutions obtained using the two alternative subgrid discretisation techniques to compute basis functions. To this end, we consider two examples. In Section 6.1, we consider a small Y-shaped synthetic sector model with three different isotropic permeability structures and discuss several fundamental numerical properties of the multiscale method. Then in Section 6.2, we consider a larger and more complex model of a layered bed on meter-scale.

In the following we will only compare the quality of the MsMFEM velocity solutions. To compare the quality of the multiscale velocity fields we will consider two error measures: (i) errors in fluxes across interfaces in the corner-point grid, and (ii) saturation errors in a two-phase flow scenario. The error in fluxes is measured as follows:

$$(25) \quad e(v) = \|(v_{\text{ref}} - v) \cdot n\|_{L^2(\partial\mathcal{T})} / \|v_{\text{ref}} \cdot n\|_{L^2(\partial\mathcal{T})}.$$

Here v_{ref} is obtained by solving (1) using the subsolver directly on the subgrid (i.e., MFDM on the corner-point grid and RT0 MFEM on the tetrahedral subgrid), v is the multiscale solution, \mathcal{T} is the corner-point grid, and n is a unit vector normal to $\partial\mathcal{T}$.

The error in fluxes (25) is not always a good indicator for the overall accuracy of a solution, especially when the velocity oscillates rapidly. We therefore also monitor the impact the errors in the velocity have on the saturation field obtained by solving a two-phase transport equation of the form,

$$(26) \quad s_t + \nabla \cdot (F_w(s)v) = \max\{f, 0\} + F_w(s) \min\{f, 0\},$$

where $F_w(s) = s^2/(2s^2 - 2s + 1)$. This nonlinear hyperbolic equation is discretised using an implicit upstream-weighted finite-volume scheme and solved using a Newton–Raphson method. For clarity, we emphasise that (26) will be solved on the *corner-point grid*. In other words, the sub-resolution inherent in the MFEM (subgrid) solver will *not* be exploited here. To assess the accuracy of the solutions of (26), we measure how much they differ from the reference solution at 0.5 PVI, i.e., we compute

$$e(s) = \|s_{\text{ref}}(\cdot, T) - s(\cdot, T)\|_{L^2} / \|s_{\text{ref}}(\cdot, T)\|_{L^2},$$

where s is the saturation induced by the MsMFEM velocity fields, s_{ref} is the saturation induced by v_{ref} , and T is defined by

$$\int_{t=0}^{t=T} \max\{f, 0\} dt = 0.5|\Omega|.$$

6.1. A Y-shaped Reservoir. The first example is a synthetic reservoir in the shape of the letter Y represented by a grid with $32 \times 32 \times 8$ blocks, see Figure 8. This grid model is much smaller than models to which one usually would apply a multiscale method. However, the size of the model is chosen on purpose to illustrate some fundamental aspects of the multiscale method.

The model is equipped with three different isotropic permeability fields: (i) homogeneous permeability; (ii) a log-normal field where the permeability values vary six orders of magnitude; and (iii) a fluvial type permeability field consisting of high-permeable channels on a low-permeable log-normal background; see Figure 8. The log-normal permeability field has been generated by sampling random numbers independently in each cell, applying a Gaussian smoothing with variance 5.0 in each direction, adjusting the variance by multiplying with a constant, and finally taking the exponential. The mean is 2.58 and the variance is 184.1. The artificial, fluvial-like permeability was generated by adding random sinusoidal curves of high permeability to a low-permeable log-normal background field. The mean is 29.0 and the variance is 2246.

We consider two different well configurations (see Figure 8): (i) an injector is placed at the base of the Y and one injector in each of the outer corners of the arms of the Y; and (ii) an injector and a producer in the two outer corners of the arms of the Y (to the right and left, respectively, in Figure 8). The pressure and velocity distributions are only computed once.

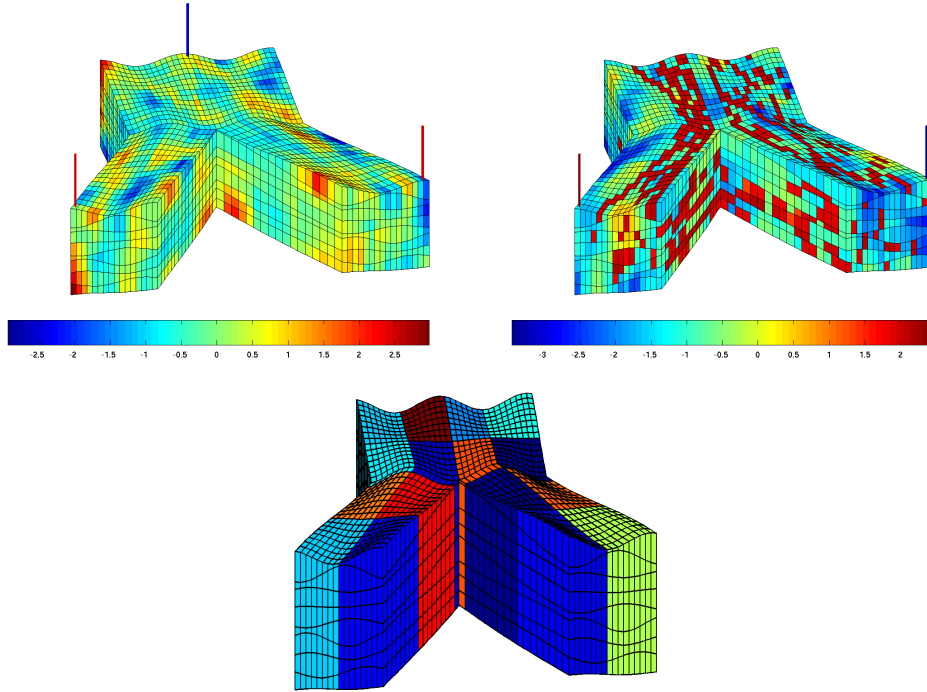


FIGURE 8. The Y-shaped reservoir: log-normal permeability field with well configuration number one (left), fluvial permeability field with well configuration number two (right), and partitioning into $4 \times 4 \times 1$ coarse blocks (bottom).

TABLE 2. Errors in fluxes and saturations for the Y-shaped reservoir computed using MsMFEM with subgrid solvers MFDM and RT0 MFEM for well configurations number one.

RT0 MFEM	Homogeneous		Log-normal		Fluvial	
	$e(v)$	$e(s)$	$e(v)$	$e(s)$	$e(v)$	$e(s)$
Coarse grid						
$16 \times 16 \times 4$	0.1233	0.0161	0.1915	0.0495	0.4069	0.2299
$8 \times 8 \times 2$	0.1300	0.0206	0.2769	0.1087	0.3845	0.2904
$4 \times 4 \times 1$	0.1070	0.0225	0.2135	0.1501	0.3046	0.2420
$2 \times 2 \times 1$	0.0112	0.0090	0.1111	0.0724	0.1564	0.0680
Mimetic FDM	$e(v)$	$e(s)$	$e(v)$	$e(s)$	$e(v)$	$e(s)$
$16 \times 16 \times 4$	0.1152	0.0193	0.1963	0.0532	0.4143	0.2278
$8 \times 8 \times 2$	0.1282	0.0213	0.3174	0.1157	0.4742	0.3607
$4 \times 4 \times 1$	0.1070	0.0249	0.2212	0.1582	0.3119	0.2442
$2 \times 2 \times 1$	0.0111	0.0103	0.1214	0.0751	0.1589	0.0679

To define the coarse grids for the multiscale method, we use a very simple strategy and partition the grid uniformly in index space. In other words, think of the geomodel as a regular $32 \times 32 \times 8$ Cartesian grid, and partition it into coarse $M_x \times M_y \times M_z$ grids, in which each coarse cell has $(32/M_x) \times (32/M_y) \times (8/M_z)$ sub-cells. Tables 2 and 3 report errors in fluxes and saturations obtained on four different coarse grids for well configurations number one and two, respectively. The results are similar for the two subgrid solvers: both for MFEM and MFDM the multiscale methodology is able to reproduce the fine-scale reference solutions with reasonable accuracy for the homogeneous and the log-normal permeability fields. In the following, we will comment more on three interesting trends in the errors for both subsolvers.

TABLE 3. Errors in fluxes and saturations for the Y-shaped reservoir computed using MsMFEM with subgrid solvers MFDM and RT0 MFEM for well configuration number two.

RT0 MFEM Coarse grid	Homogeneous		Log-normal		Fluvial	
	$e(v)$	$e(s)$	$e(v)$	$e(s)$	$e(v)$	$e(s)$
$16 \times 16 \times 4$	0.1502	0.0270	0.2281	0.0486	0.4191	0.2533
$8 \times 8 \times 2$	0.1554	0.0550	0.2937	0.0821	0.3633	0.2650
$4 \times 4 \times 1$	0.1756	0.1428	0.2081	0.1263	0.2942	0.2668
$2 \times 2 \times 1$	0.2509	0.3570	0.2812	0.3638	0.1892	0.1771
Mimetic FDM	$e(v)$	$e(s)$	$e(v)$	$e(s)$	$e(v)$	$e(s)$
$16 \times 16 \times 4$	0.1409	0.0266	0.2307	0.0478	0.4215	0.2440
$8 \times 8 \times 2$	0.1567	0.0584	0.3472	0.0934	0.4466	0.3331
$4 \times 4 \times 1$	0.1776	0.1527	0.2097	0.1302	0.2974	0.2711
$2 \times 2 \times 1$	0.2537	0.3735	0.2810	0.3720	0.1846	0.1799

In Table 2, we see that the best resolution is obtained with the smallest and largest coarse grids for the homogeneous and log-normal permeability fields. For the $16 \times 16 \times 4$ coarse grid, the coarse-scale system is able to resolve the majority of the global flow. Similarly, for the $2 \times 2 \times 1$ coarse grid, the multiscale basis functions are able to capture most of the flow pattern in the arms and the leg of the Y. For the other two coarse grids, the coarse-scale system is too small to capture the global flow accurately and the local fine-scale systems are too small to represent the (global) flow patterns accurately in the multiscale basis functions. Previous experience with MsMFEM on Cartesian grids indicate that typical upscaling factors of 4–16 in each direction are the most computationally feasible, giving local problems with between 100 and 1 000 cells.

The flow pattern for the fluvial permeability field is dominated by high-permeable heterogeneous structures that have the same length scale as the whole reservoir. The flow patterns represented in the multiscale basis functions are restricted locally to each pair of coarse-grid blocks by the assumption of no-flow boundary conditions on the local flow problems. In other words, the local flow problems are not able to accurately resolve and represent the long correlation structures in the high-permeable channels. This is reflected in Tables 2 and 3, where one can observe that the resolution is improved by increasing the size of the coarse blocks. For fluvial, and other heterogeneities with long correlation lengths, a better approach would be to use *global boundary conditions* to define the multiscale basis functions. That is, to use a single initial pressure solution on the fine grid to compute representative boundary conditions for the local flow problems; see e.g., [2]. This way, the multiscale basis functions are able to represent local parts of flow patterns extending beyond a single cell in the coarse grid.

For the second well configuration, the velocity profile has a sharp turn at the intersection of the two arms of the Y. The basis functions are formed by driving a unit flow from one grid-block to its immediate neighbour, and as such have no natural representation of flow fields turning ninety degrees. This is particularly true for the homogeneous case, where the multiscale basis functions will correspond roughly to the RT0 basis functions on the coarse grid. The sharp turn at the intersection will therefore be more smeared out as the size of the cells in the coarse-grid increases. Hence, the resolution deteriorates when the size of the coarse blocks increases, as observed for the homogeneous and log-normal permeabilities in Table 3.

6.2. A Wavy Depositional Bed. In the second example we consider a corner-point grid modelling a wavy depositional bed on a meter-scale. The corner-point grid has vertical pillars that form a uniform 30×30 grid in the horizontal plane. The model has 100 very thin layers, of which many collapse to a hyper-plane in some regions; see Figure 9. The grid has 29 629 active cells originally. However, thirty-one of the cells have a degeneracy as in the lower-right plot in Figure 2. If we assume that all corner-point cells are unions of tetrahedra as in the tetrahedral MFEM subgrid, the two internal parts of each of these thirty-one cells are only connected through a single line (i.e., through an interior interface of zero area). These cells are therefore split into

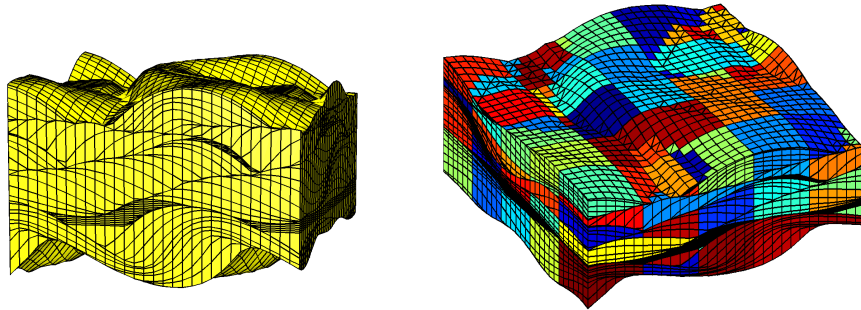


FIGURE 9. Corner-point grid for the wavy depositional bed: original grid (left) and the partition into a $5 \times 5 \times 10$ coarse grid (right)

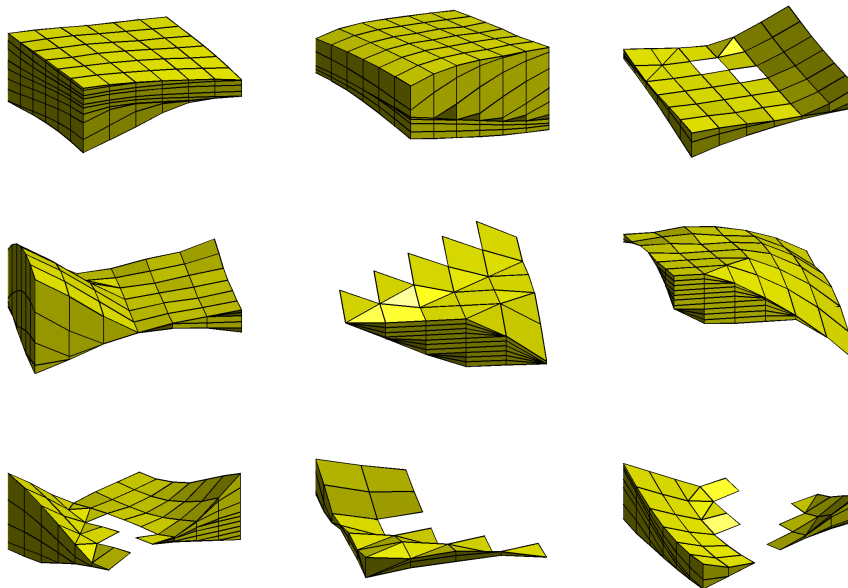


FIGURE 10. Nine different coarse cells arising from a uniform partitioning of the wave-bed model in index space. In the plot, strongly curved cell faces have been split into triangles.

two cells each, giving a grid that altogether consists of a total of 29 660 cells. The total number of tetrahedra in the tetrahedral MFEM subgrid is 147 334.

As in the previous example, we apply a uniform partition in index space to obtain the $M_x \times M_y \times M_z$ coarse grids, where each cell consists of $(30/M_x) \times (30/M_y) \times (100/M_z)$ sub-cells. However, unlike the previous example, we now obtain cells that have zero volume, cells that are disconnected, and cells that contain internal holes; see Figure 10. Each disconnected coarse cell is split into a subcollection of connected cells, coarse cells with zero volume are removed, and all other cells are left unchanged.

An alternative grid generation approach would be to partition the grid in physical space rather than in index space. In other words, to divide the physical space into a set of uniform hexahedral cells and define each coarse cell as distinct unions of cells preserving the volume of the hexahedral cells as close as possible. Using this approach, the cells would have a cubic-like shape, but the surface of the cells would become more irregular. We intend to investigate more closely how to develop a good strategy for choosing coarse grids in future work.

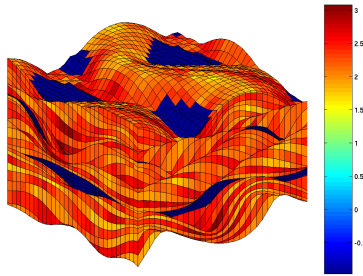


FIGURE 11. Logarithm of the heterogeneous, isotropic permeability field for the wavy bed. The permeability varies between 0.10 mD and 1.69 D, with mean 94.9 mD and standard deviation 0.22.

TABLE 4. Errors in fluxes and saturations for the wavy depositional bed computed using the MsMFEM with subgrid solver MFDM (top) and RT0 MFEM (bottom).

RT0 MFEM	Isotropic K		Anisotropic K		Heterogeneous K	
	$e(v)$	$e(s)$	$e(v)$	$e(s)$	$e(v)$	$e(s)$
Coarse grid						
$10 \times 10 \times 10$	0.1910	0.0223	0.2314	0.1434	0.1967	0.0912
$6 \times 6 \times 2$	0.1256	0.0412	0.2030	0.1734	0.1499	0.1456
$3 \times 3 \times 1$	0.0607	0.0653	0.0931	0.1300	0.0793	0.1077
Mimetic FDM	$e(v)$	$e(s)$	$e(v)$	$e(s)$	$e(v)$	$e(s)$
$10 \times 10 \times 10$	0.2028	0.0264	0.2485	0.1427	0.2152	0.0941
$6 \times 6 \times 2$	0.1302	0.0420	0.2071	0.1691	0.1547	0.1406
$3 \times 3 \times 1$	0.0624	0.0651	0.0948	0.1271	0.0807	0.1057

We now consider three different permeability fields; a homogeneous and isotropic field; a homogeneous and anisotropic field for which K is diagonal with $k_{xx} = k_{yy} = 1000$ and $k_{zz} = 1$; and a heterogeneous and isotropic field for which the permeability in each layer is log-normal, see Figure 11. Although our grid geometry originally models a depositional bed, we here use it as a sector model and specify a standard quarter-five-spot flow scenario with injection in the first vertical column and production in the last vertical column of the grid. Table 4 reports the corresponding errors in fluxes and saturation obtained on three different coarse grids. The good resolution of the two multiscale solvers is amazing, given the complex shapes of the coarse-grid blocks as depicted in Figure 10.

7. Concluding Remarks

Multiscale methods have become popular among researchers in many engineering disciplines. Nevertheless, multiscale methods are generally regarded as immature, and few, if any, have penetrated into industrial use. In this paper we have tried to promote the use of multiscale methods for flow simulation of geometrically complex and highly heterogeneous reservoir models. To this end, we have extended the multiscale finite-element method (MsMFEM) to corner-point grids, which is the grid format used by most commercial geomodelling software and reservoir simulators to model porous rock formations containing producible hydrocarbon.

The numerical results presented in the paper demonstrate that the multiscale mixed finite-element method provides detailed and quite accurate velocity fields and saturation profiles for two-phase simulations on typical geomodels arising in real-life reservoir engineering. Combined with previous results on Cartesian grids [1, 2, 3], we believe that these results demonstrate that the multiscale mixed finite-element formulation is a versatile and robust alternative to the traditional upscaling/downscaling approach used in the petroleum industry. For a further comparison of

various state-of-the-art upscaling and multiscale methods we refer the reader to another paper in this special issue [14].

A particular advantage of the multiscale mixed formulation is its ease of implementation. Given a proper discretisation methodology on the underlying corner-point grid, it is straightforward to implement the multiscale mixed method on top of the existing pressure solver. In fact, our coarse-grid Matlab code used in Section 6—including grid processing, hybrid formulation, and linear algebra—only consists of about 200 code lines. Implementing MsMFEM in a commercial solver should therefore not be a daunting task.

Another advantage of the MsMFEM formulation is the ease with which one handles the coarse grids. In particular, we have demonstrated how one can avoid the difficulties of resampling that are usually encountered in grid coarsening, since the multiscale mixed formulation allows the cells in the coarse grid to be chosen as an (almost) arbitrary connected collection of cells in the underlying geological model. We believe that this will prove to be very advantageous when considering more complex geomodels containing fractures and faults, for which the corresponding geological models will generally be non-conforming and therefore have non-matching interfaces. In ongoing research we try to extend the multiscale formulation to industry-standard geological models with fractures/faults and non-conforming fine grids.

In summary, we believe that the multiscale mixed finite-element method can greatly facilitate flow simulation on complex grid models and potentially be used to perform two-phase flow simulations directly on full-scale geological models.

In the current paper, the multiscale mixed formulation was used in combination with two different subgrid solvers that both aim to give accurate and robust discretisations with minimal grid-orientation effects on grids with strong anisotropies and irregular geometries. Although both subgrid solvers give good results, the results obtained with the recent mimetic formulation are particularly promising and encourage further development towards future use within reservoir simulation. Mimetic methods work directly on the corner-point grid, can be formulated for general polyhedral cells with curved faces, and are easy to implement. Moreover, our (limited) experience indicates that they are quite robust with respect to the anisotropies and geometrical complexities encountered in industry-standard corner-point grids.

Acknowledgement

The research of Aarnes, Krogstad, and Lie is funded by the Research Council of Norway under grants no. 158908/I30 and 162606/V30. The research of Laptev is funded by an ERCIM postdoctoral grant. The corner-point grid used in Section 6.2 is generated with SBEDTM, and has been provided by Alf B. Rustad at STATOIL.

References

- [1] J. E. Aarnes. On the use of a mixed multiscale finite element method for greater flexibility and increased speed or improved accuracy in reservoir simulation. *Multiscale Model. Simul.*, 2(3):421–439, 2004.
- [2] J. E. Aarnes, V. Kippe, and K.-A. Lie. Mixed multiscale finite elements and streamline methods for reservoir simulation of large geomodels. *Adv. Water Resour.*, 28(3):257–271, 2005.
- [3] J. E. Aarnes, S. Krogstad, and K.-A. Lie. A hierarchical multiscale method for two-phase flow based upon mixed finite elements and nonuniform coarse grids. *Multiscale Model. Simul.*, 5(2):337–363, 2006.
- [4] I. Aavatsmark, T. Barkve, Ø. Bøe, and T. Mannseth. Discretization on unstructured grids for inhomogeneous, anisotropic media. part i: Derivation of the methods. *SIAM J. Sci. Comp.*, 19(5):1700–1716, 1998.
- [5] I. Aavatsmark, T. Barkve, Ø. Bøe, and T. Mannseth. Discretization on unstructured grids for inhomogeneous, anisotropic media. part ii: Discussion and numerical results. *SIAM J. Sci. Comp.*, 19(5):1717–1736, 1998.
- [6] D. N. Arnold and F. Brezzi. Mixed and nonconforming finite element methods: implementation, postprocessing and error estimates. *RAIRO Modél. Math. Anal. Numér.*, 19(1):7–32, 1985.
- [7] F. Brezzi, K. Lipnikov, and M. Shashkov. Convergence of mimetic finite difference methods for diffusion problems on polyhedral meshes. *SIAM J. Num. Anal.*, 43:1872–1895, 2005.
- [8] F. Brezzi, K. Lipnikov, and M. Shashkov. Convergence of mimetic finite difference methods for diffusion problems on polyhedral meshes with curved faces. *Math. Models Methods Appl. Sci.*, 16(2):275–297, 2006.
- [9] F. Brezzi, K. Lipnikov, M. Shashkov, and V. Simoncini. A new discretization methodology for diffusion problems on generalized polyhedral meshes. LAUR-05-8717, Report of Los Alamos National Laboratory, <http://cnls.lanl.gov/~shashkov/>, 2005.

- [10] F. Brezzi, K. Lipnikov, and V. Simoncini. A family of mimetic finite difference methods on polygonal and polyhedral meshes. *Math. Models Methods Appl. Sci.*, 15:1533–1553, 2005.
- [11] Z. Chen and T. Hou. A mixed multiscale finite element method for elliptic problems with oscillating coefficients. *Math. Comp.*, 72:541–576, 2003.
- [12] M. Edwards, R. Lazarov, and I. Yotov (eds.). Special issue on locally conservative numerical methods for flows in porous media. *Comp. Geosci.*, 6(3-4):225–579, 2002.
- [13] T. Hou and X.-H. Wu. A multiscale finite element method for elliptic problems in composite materials and porous media. *J. Comput. Phys.*, 134:169–189, 1997.
- [14] V. Kippe, J. Aarnes, and K.-A. Lie. A comparison of multiscale methods for elliptic problems in porous media flow. *Comp. Geosci.*, 2006, submitted.
- [15] D. K. Ponting. Corner point geometry in reservoir simulation. In P. King, editor, *Proceedings of the 1st European Conference on Mathematics of Oil Recovery, Cambridge, 1989*, pages 45–65, Oxford, July 25–27 1989. Clarendon Press.

(Aarnes, Krogstad, Lie)

SINTEF ICT, DEPT. APPLIED MATHEMATICS, P.O. BOX 124 BLINDERN, N-0314 OSLO, NORWAY.

[HTTP://WWW.MATH.SINTEF.NO/GEOSCALE/](http://www.math.sintef.no/geoscale/)

E-mail address: {jaa, steink, knl}@sintef.no

(Laptev)

DEPARTMENT OF MATHEMATICAL SCIENCES, NTNU TRONDHEIM, N-7491 TRONDHEIM, NORWAY